Structural, Morphological, Optical and Electrical Properties of CuO Nanostructures Undoped and Doped with Silver

M. Zerouali[a,*], R. Daïra[a], D. Bouras[b], B. Boudjema[a] and B. Régis[c]

[a] *LRPCSI, University of 20 Août 1955 Skikda, P.B. 26, Route d'El-Hadaiek, 21000 Skikda, Algeria*
[b] *Department of Science of Matter, Faculty of Science and Technology, University of Souk-Ahras, 41000 Souk Ahras, Algeria*
[c] *MOLTECH-Anjou, University of Angers/UMR CNRS 6200, 2 Bd Lavoisier, 49045 Angers, France*

Received: 17.04.2024 & Accepted: 28.08.2024

Doi: 10.12693/APhysPolA.146.304 *e-mail: m.zerouali@univ-skikda.dz

Copper oxide thin films undoped and doped with silver (15 wt%, 25 wt%) were deposited by two different methods, namely sol–gel dip coating and sol–gel spin coating, on a glass substrate with a 0.2 M precursor concentration. The samples are characterized by X-ray diffraction, Fourier-transform infrared spectroscopy, scanning electron microscopy, energy-dispersive X-ray, UV-visible spectrophotometry, and the four-point probe method. Structural, morphological, optical, and electrical properties of Ag-doped CuO are studied. According to the X-ray diffraction spectroscopy, all peaks confirm the formation of the tenorite phase with a monoclinic structure. The thin films were all polycrystalline with directions along (200). According to scanning electron microscopy, the morphology of the films is almost smooth. A comparison is made between the two techniques of fabrication in terms of electric conductivity, morphology, energy gap, and average transmission in the visible domain.

topics: copper oxide, doped silver, dip coating, spin coating

1. Introduction

Transition metal oxides have focused the interest of researchers in recent years due to their characteristics [1], including a diverse set of electrical, chemical, and physical properties that are frequently sensitive to changes in their chemical environment [2]. Copper oxide (CuO) has attracted the interest of many researchers due to many potential applications in solar energy devices, gas sensors, nanowires, magnetic storage, Li-ion batteries, photocatalysis, infrared photodetectors, electrochemical sensors, field emitters, antibacterials, and superconductors [3–6].

CuO is an ideal choice as an environmental sensor thanks to its effective properties such as a high absorption coefficient, good thermal conductivity [7], non-toxicity [8], low cost, and good adaptation to the environment [9]. This material is part of the group II–VI [10], a p-type semiconductor with a band gap of 1.2–2.1 eV and crystallizes into a monoclinic crystal structure [11–13] with lattice parameters $a = 4.684$ Å, $b = 3.425$ Å, $c = 5.129$ Å, and $\beta = 99.28$ Å [14]. Copper oxide films have been prepared using various deposition techniques, such as pyrolysis spray [15], sol–gel [16, 17], direct current (DC) reactive sputtering [18], and thermal evaporation [19]. Moreover, gas sensors based on p-type semiconductors such as CuO have recently gained popularity due to their chemical stability, electrochemical activity, and strong electron communication capabilities [20]. The novelty of forming nanostructures via dip and spin coating lies in the method's ability to achieve controlled and precise fabrication, contrasting with traditional thermal or electrochemical techniques, which often yield larger nanostructures with inferior aspect ratios. Dip coating involves immersing substrates in a precursor solution, ensuring uniform coating through capillary action upon withdrawal, while spin coating deposits a thin liquid film onto a rotating substrate using centrifugal force [11]. This versatile manufacturing method offers advantages such as precise control over coating thickness and uniformity, making it ideal for creating nanostructures with consistent properties. It is cost-effective and scalable from small lab-scale experiments to large-scale

production, enabling broader commercial applications. However, dip and spin coating is primarily suited for thin films, posing challenges for producing thicker nanostructures or complex three-dimensional architectures. Compared to thermal and electrochemical methods commonly used for CuO/Cu_2O synthesis, the dip and spin coating provides superior aspect ratio control, simplicity, and high uniformity, critical for applications in catalysis, sensors, and biomedical devices where consistent performance is essential [12, 13]. Spin coating provides a high degree of uniformity in thin film formation. The centrifugal force ensures that the coating spreads evenly across the substrate, leading to highly uniform nanostructures, but dip coating offers excellent control over the thickness and morphology of the coating [15]. The withdrawal speed and solution concentration can be precisely managed to achieve the desired properties. Both spin and dip coating are relatively simple and scalable processes. They do not require complex equipment or conditions, making them cost-effective and easy to implement in large-scale production [18]. These methods are versatile and can be used to deposit a wide range of materials, including various oxides, polymers, and composites. Such flexibility is often limited in thermal or electrochemical methods, which may require specific conditions for each material [19]. Spin and dip coating typically involves lower temperatures compared to thermal methods. This is beneficial for substrates that cannot withstand high temperatures, thus expanding the range of usable substrates [16–20].

CuO has a high sensitivity to hydrogen sulfide (H_2S). Gas sensors have received a lot of interest as integrated devices in daily life for accurate monitoring and control of ambient moisture for human comfort, as well as prospective applications in sectors such as robotics, aerospace, agriculture, and healthcare [21]. CuO might be employed as a sensor for other gases, such as carbon monoxide (CO) and nitrogen dioxide (NO_2). Early detection of these gases is especially important in industrial processes, factories, and homes [22].

For the preparation of thin films, various methods can be used, namely sol–gel spin coating, DC sputtering, electrodeposition, or spray pyrolysis technique. The aim of this study is to characterize the structural, morphological, optical, and electrical properties of copper oxide thin films undoped and doped with silver and deposited by two different methods, namely sol–gel dip coating and sol–gel spin coating, on a glass substrate. The most commonly used technique is the sol–gel method due to its simplicity, lower cost, reproducibility, and large-area deposition. The sol–gel method can easily deposit the material on different types of substrates and can be performed in a non-vacuum environment. However, another simple, low-cost, and well-spread technique can be used to obtain thin films. The obtained results show that sample surface morphology and conductivity changed as a function of the different deposition methods. Moreover, with the spin coating method, the transmittance spectrum of thin layers is weak, which confirms that thin films of CuO undoped and doped with silver are absorbent layers for solar cells and sensors.

2. Experimental details

2.1. Materials

The $Cu(CH_3COO)_2 \cdot 2H_2O$ (dehydrated copper acetate) supplied by Chemical Biochemistry, France, along with absolute ethanol (C_2H_6O, 96% purity) and monoethanolamine (MEhlA, $NH_2CH_2CH_2OH$, $\geq$ 98% purity) from Sigma-Aldrich, USA, were utilized for solution preparation. Silver nitrate ($AgNO_3$, 99% purity) from Chemical Biochemistry, France, was employed for doping purposes.

2.2. Preparation of solutions and thin films

CuO thin films were deposited with a sol–gel (spin coating and dip coating) method on glass substrates (Fig. 1). For this purpose, a 0.2 M molarity solution was prepared by dissolving dehydrated copper acetate precursor ($Cu(CH_3COO)_2 \cdot 2H_2O$) in absolute ethanol ($C_2H_6O$ purity 96%). In order to study the effect of Ag doping rate on CuO thin films, one volume of monoethanolamine (MEA) in a molar ratio ($n(\text{MEA})/n(\text{sol}) = 3$) was added to two solutions with different silver percentages (15 wt%, 25 wt%) with silver nitrate precursor. The solutions were then mixed under magnetic stirring at 70°C for 2 h. In spin coating, the substrates are mounted on the substrate at a rotating speed of 3000 rpm for 30 s and then dried after each deposition at 250°C for 10 min in the oven (repeated for 4 cycles). In dip coating, the substrate is left in the solution for 1 min (repeated for 15 cycles. Then, we take the samples for heat treatment in the oven at 500°C for 2 h.

2.3. Characterization techniques

To study the structural properties of thin layers of pure and Ag-doped CuO, an X-ray diffraction (XRD) platform (Brucker AXS D8 ADVANCE) with a Cu K_α radiation diffractometer ($\lambda = 1.54$Å) was used. The film morphology was examined using an environmental scanning electron microscope (SEM) (Thermo Scientific Prisma E). Infrared (IR) transmission spectra were recorded using a VERTEX 70 spectrophotometer in the spectral range of 400–1000 cm^{-1}. The transmittance spectra were obtained using a UV-visible spectrophotometer

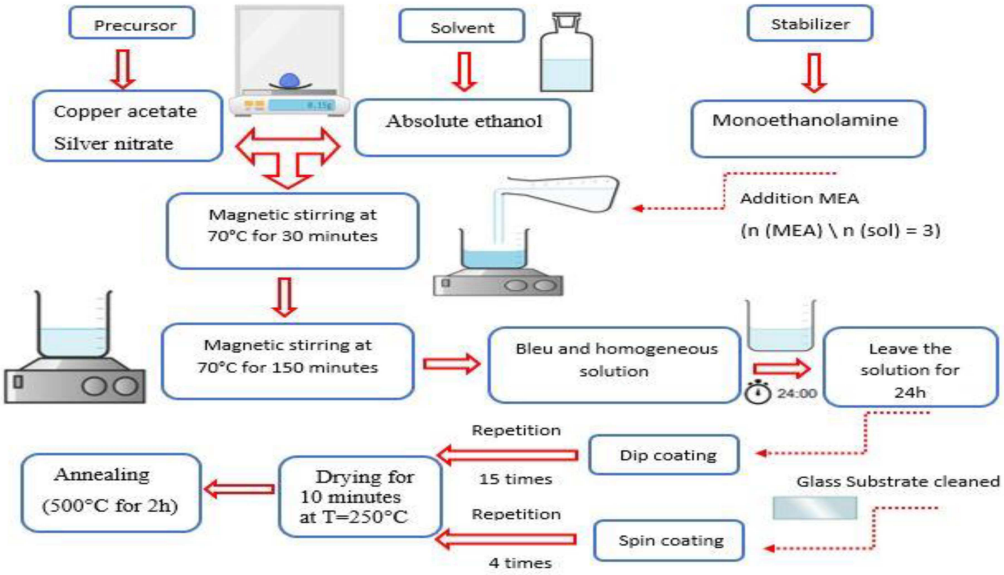

Fig. 1. Different steps of preparation of the solution for dip coating or spin coating method.

(JASCO V-750 in the wavelength range between 350–900 nm. The electrical properties were measured with a four-point measuring device (JANDEL) connected to a Keithley 2400 source meter.

3. Results and discussion

3.1. X-ray diffraction

Undoped and doped silver copper oxide thin films prepared by the sol–gel method (dip and spin coating) were characterized by X-ray diffraction to study their structural properties.

Figure 2a presents the XRD spectra of thin films prepared by the dip coating method. The spectra are recorded in the range of 2θ from 25° to 80°. It has been noted that in all the spectra, there are several peaks of diffractions that correspond to the following planes: (−111), (200), (−202), (202), (−113), (022), (−222). The results are in good agreement with the JCPDS sheet no. 00-041-0254 and show the polycrystalline nature of the monoclinic structure, which belongs to the $C2/c$ space group as a pure phase. No secondary phase of Cu_2O or Cu_4O_3 is observed. For silver-doped samples, the intensity of the planes (−111), (−202), (202), (−113) decreases with the increase in the doping rate. On the other hand, for the planes (200), (022), (−222), the peak intensity is increased with the increase in the doping rate. A secondary peak (440) is consistent with the JCPDS card no. 00-040-0909, indicating the formation of silver oxide Ag_2O_3. A well-defined plane is shifted towards the smaller angles in the case of Ag doping. The result explains that the Ag atoms occupy the substitution sites of Cu atom because CuO, in the absence of metal caused by cationic vacancies, releases holes and makes the material a p-type semiconductor. The compression of the mesh reduces the unit volume of the cell (the parameters of the mesh decrease with the existence of doping (see Table I)).

Figure 2b represents XRD spectra of undoped and Ag-doped copper oxide thin films recorded in the range of 2θ from 20° to 70°. These layers are prepared by the sol–gel method (spin coating). It presents diffraction peaks associated with the following crystalline planes (110), (−111), (200), (020), (−202), (202), (−113), (−311). The outcomes are consistent with reported data [23, 24]. The results are in agreement with JCPDS card no. 00-041-0254, which confirms the existence of a monoclinic tenorite phase with a $C2/c$ space group structure. Additional peaks are present, corresponding to the appearance of secondary phases associated with CuO films doped with Ag atoms. Three diffraction peaks at $2\theta = 27.77°$, 37.88°, 45.99°, and 64.55° correspond to the (110), (200), (211), and (311) planes, respectively. They provide evidence for the presence of the Ag_2O phase and agree well with the JCPDS card no. 00-041-1104. The peak at $2\theta = 44.25°$ corresponding to the (440) plane is in agreement with the JCPDS card no. 00-040-0909, indicating the formation of silver oxide Ag_2O_3. It should be noted that there are shifts of the peaks towards small angles, which shows the compression in the lattice.

The value of the texture coefficient provides crucial details regarding the preferred orientation of the thin films. The Harris analysis is used to determine the texture coefficient (T), which confirms the preferred orientation [25]

$$\mathrm{T}_{C_{hkl}} = \frac{I_{hkl}}{I_{0;hkl}} \Big/ \left(\frac{1}{N} \sum \frac{I_{hkl}}{I_{0;hkl}} \right). \quad (1)$$

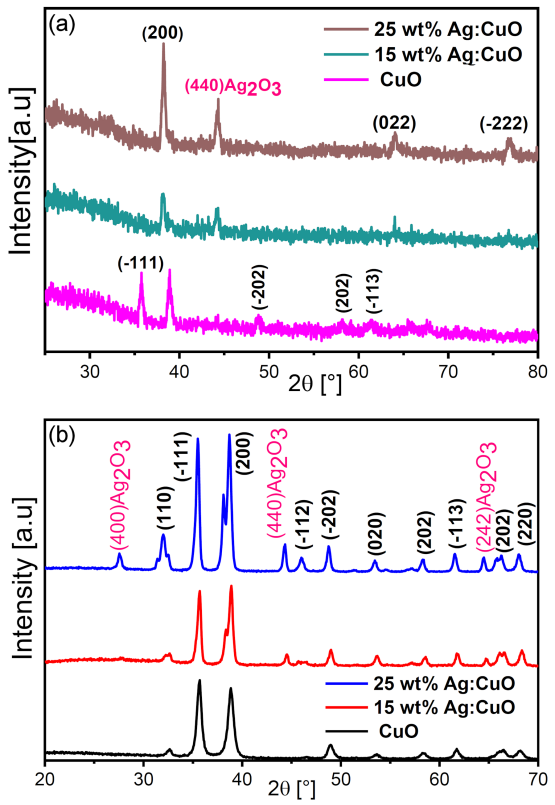

Fig. 2. XRD spectra of Ag-doped CuO thin films prepared by (a) sol–gel dip coating and (b) spin coating.

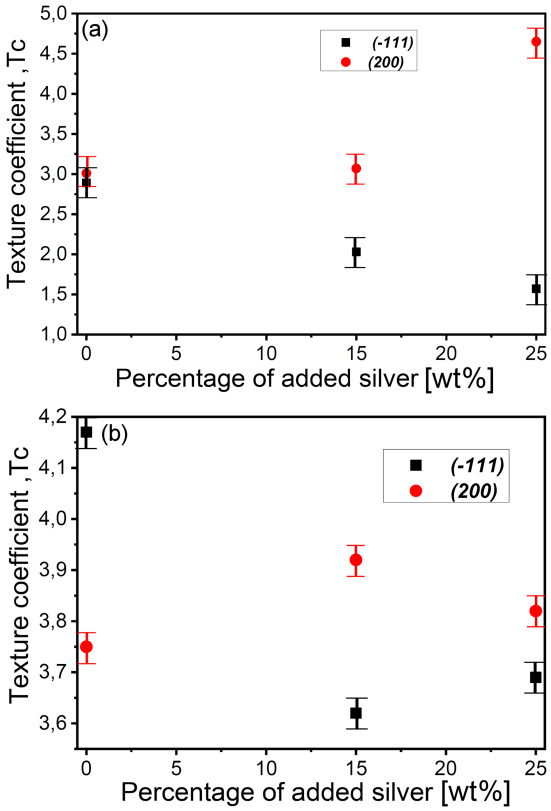

Fig. 3. Texture coefficient at (−111) and (200) as a function of the doping rate for dip coating (a) and spin coating (b) method.

Here, $T_{C_{hkl}}$ is the texture coefficient of the (hkl) plane, I_{hkl} is observed intensity, $I_{0;hkl}$ is the reference intensity of the (hkl) plane, and N is the number of peaks considered.

For $0 < T < 1$, there are not enough grains moving in the direction under consideration $(h_i k_i l_i)$, and there is no preferential orientation. If $T > 1$ for each of the $(h_i k_i l_i)$ planes that have been observed, the value of T indicates that more grains are oriented in a particular direction $(h_i k_i l_i)$, making that direction the preferred orientation [26].

Figure 3a and b represents the texture coefficient. Two preferential orientations are observed and follow the planes (200) and (−111). The plane (200) is more intense in all the thin layers when the samples are prepared by the dip coating method. On the other hand, for thin layers prepared by the spin coating method, there is a change in the intensity of the peaks with the doping. This effect is explained by the position of the atoms in these low-energy sites and shows the increase in the intensity of the peaks with a decrease in the full width at half height maximum (FWHM).

The crystallite size was calculated by Scherrer's formula [27, 28]

$$D = \frac{0.9\,\lambda}{\beta\,\cos(\theta)}, \tag{2}$$

where D is the crystallite size, λ is the wavelength of the incident ray, β is the full width at half height maximum (FWHM), and θ is the Bragg diffraction angle.

The dislocation density (δ) is explained by the length of the dislocation lines per unit volume of the crystal [29]; it is determined from the following relationship

$$\delta = \frac{1}{D^2}. \tag{3}$$

The micro-strain (ε) created in the thin films was calculated by equation [30]

$$\varepsilon = \frac{\beta\,\cos(\theta)}{4}. \tag{4}$$

The lattice parameters ($a \neq b \neq c$, $\alpha = \gamma = 90° \neq \beta$) of the monoclinic structure of CuO were calculated using the following relations [31]

$$\frac{1}{d^2} = \frac{1}{\sin^2(\beta)}\left[\frac{h^2}{a^2} + \frac{k^2\sin^2(\beta)}{b^2} + \frac{l^2}{c^2} - \frac{2hl\cos(\beta)}{a\,c}\right]. \tag{5}$$

Table I represents the crystallite size values. It should be noted that the size of the crystallites is nanometric and varies: 20, 25, and 29 nm for thin layers prepared by the dip coating method. However, in the case of preparation by spin coating, the size of the crystallites is 24, 33, and 28 nm and

TABLE I

The crystallite size and lattice parameters of thin films of copper oxide undoped and doped with Ag prepared by two methods

Phases	2θ [°]	Plane (hkl)	FHWM [°]	β [rad]	a [Å]	b [Å]	c [Å]	D [nm]	$\delta(\times 10^{15})$ [lines/m^2]	ε $(\times 10^{-4})$
Dip coating method										
CuO	38.95	(200)	0.404	0.0071	4.692	3.428	5.144	20	2.5	17.75
15 wt% Ag:CuO	38.80	(200)	0.340	0.0059	4.688	3.417	5.143	25	1.6	14.75
25 wt% Ag:CuO	38.82	(200)	0.289	0.0051	4.682	3.452	5.140	29	1.19	12.75
Spin coating method										
CuO	38.85	(200)	0.394	0.0068	4.698	3.417	5.119	24	1.74	17
15 wt% Ag:CuO	38.81	(200)	0.294	0.0051	4.709	3.426	5.075	33	0.92	12.75
25 wt% Ag:CuO	38.71	(200)	0.344	0.0060	4.709	3.426	5.102	28	1.28	15

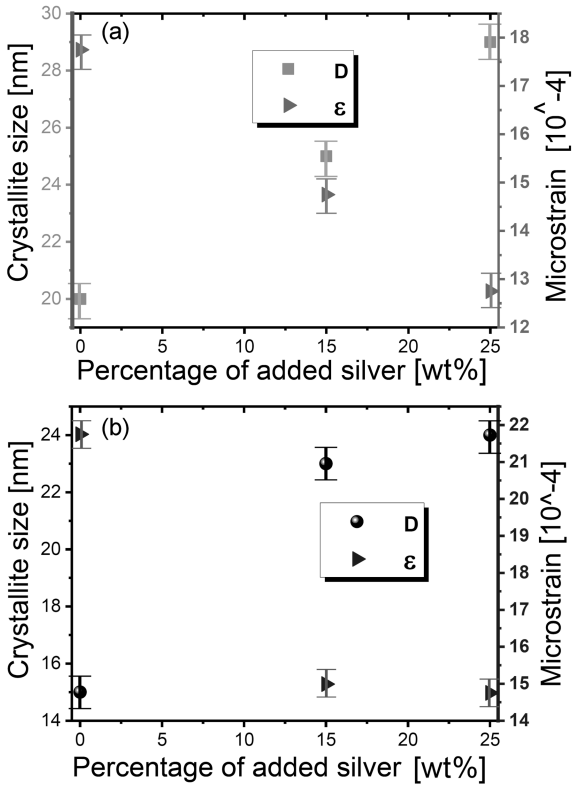

Fig. 4. Crystallite size and microstrain of copper oxide undoped and doped with Ag by two methods as a function of the doping rate.

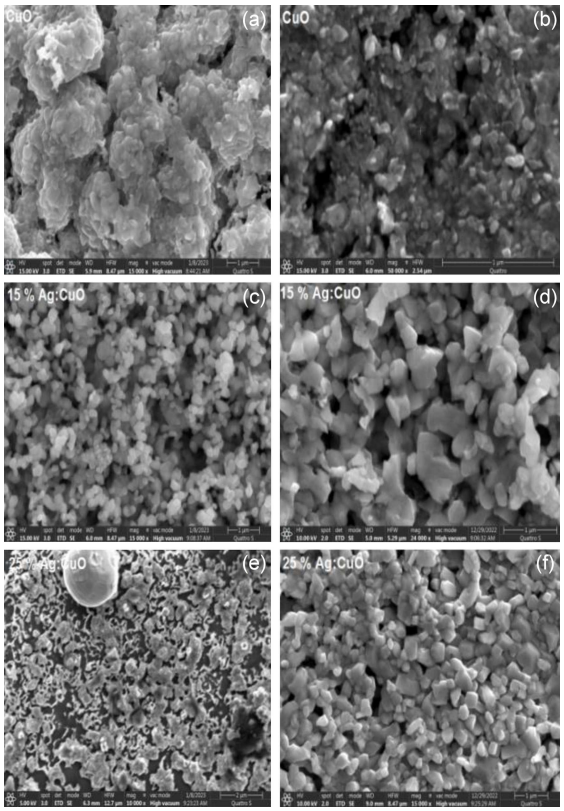

Fig. 5. SEM image of CuO and Ag:CuO deposited by (a) sol–gel dip coating and (b) spin coating.

corresponds to pure CuO, 15 wt% Ag:CuO, and 25 wt% Ag:CuO, respectively. They are very close to the result reported by H. Absike et al. [32]. It should be noted that the growth rate of the thin films prepared by dip coating is fast compared to the speed of the growth rate of the films prepared by spin coating. It should also be noted that the size of the crystallites increases with the increase in the doping rate. This explains why there is an increase in nucleation sites with doping. It also leads to a decrease in the size of the crystallites and to the phenomenon of recrystallization, i.e., "the fusion of smaller crystallites for the formation of large crystallites" and growth [33]. The size of the crystallites increases. There are several similar studies on the effect of increasing crystallite sizes with doping with silver atoms [34, 35].

Moreover, XRD results are exploited to determine other parameters, such as the density of dislocations and micro-deformations. It should be noted that the dislocation and micro-deformation decrease with the increase in the sizes of the

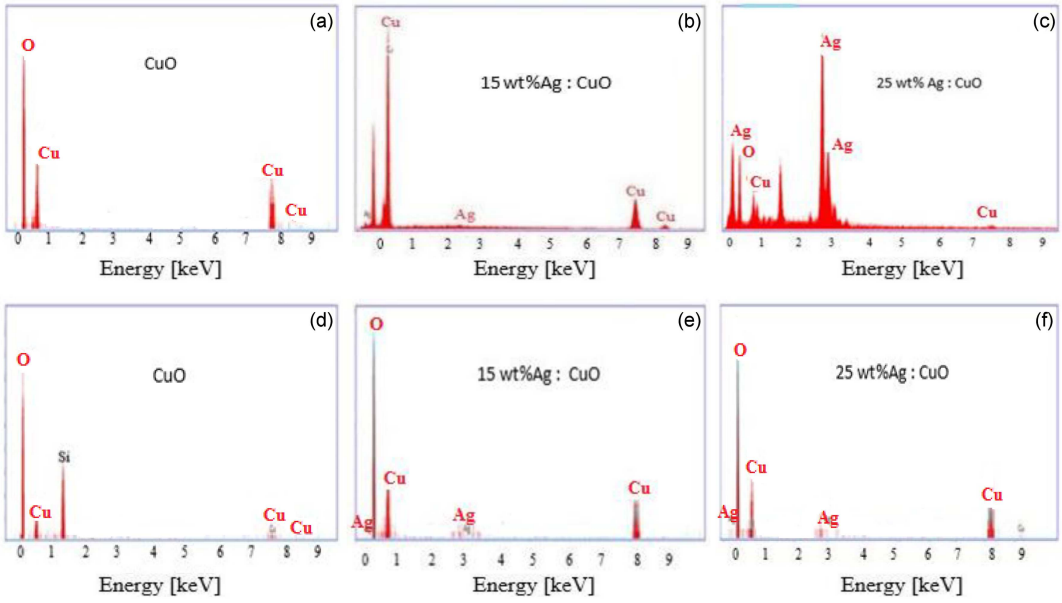

Fig. 6. EDX analysis spectrum of CuO and Ag:CuO deposited by (a–c) sol–gel dip coating and (d–f) spin coating.

crystallites [36, 37] (see Fig. 4a and b). This decrease in the micro-deformation and the density is attributed to the reduction of lattice defects along grain boundaries [38].

3.2. Morphological properties

SEM has been used to study the surface morphology of thin films of undoped and silver-doped copper oxide. As presented in Fig. 5, there is a clear change in the morphology of undoped CuO and Ag-doped CuO in the case of the dip coating method. CuO films have a smaller grain size. After Ag doping, an improvement in the morphology with an almost smooth surface is observed. For the spin coating method (panel b), all films are dense and thick and have surfaces with homogeneous and almost uniform grain sizes with a spherical shape.

The advantage of forming nanostructures with Ag/CuO using dip and spin coating methods, compared to larger structures like CuO/Cu_2O nanoneedles produced via thermal or electrochemical methods, lies in their superior control over morphology, composition, and surface properties [23]. Dip and spin coating techniques enable precise deposition and formation of well-defined nanostructures with higher aspect ratios, leading to increased surface area per unit volume. This enhanced surface area is advantageous for applications requiring efficient surface interactions, such as catalysis and sensing [24]. Furthermore, these methods offer scalability, uniformity, and compatibility with industrial processes, facilitating easier integration into devices and systems compared to larger, less controllable structures. Overall, nanostructures formed via dip and spin coating exhibit enhanced performance and tailored properties that are beneficial for various technological applications [24, 25].

TABLE II

The ratio of CuO undoped and Ag-doped chemical components.

Phases	Cu [%]	O [%]	Ag [%]
CuO^a	86.75	13.25	0
CuO^b	50	33.12	0
15 wt% $Ag:CuO^a$	85.81	12.53	1.65
15 wt% $Ag:CuO^b$	80.57	17.61	1.82
25 wt% $Ag:CuO^a$	5.76	12.62	81.62
25 wt% $Ag:CuO^b$	79.23	16.94	3.84

Thin films prepared by ^{a}sol–gel dip coating and ^{b}sol–gel spin coating.

3.3. EDX analysis

Energy dispersive X-ray (EDX) analysis was utilized to determine the quantity of the elements and confirm their presence in the thin films. Figure 6 depicts the EDX spectra of CuO and Ag:CuO thin films with varying doping percentages. The Cu and O peaks may be seen throughout the sample. The presence of additional Ag peaks also increases with the increase in the doping rate (0.71% for doping with 15 wt% Ag and 46.25 % for doping with

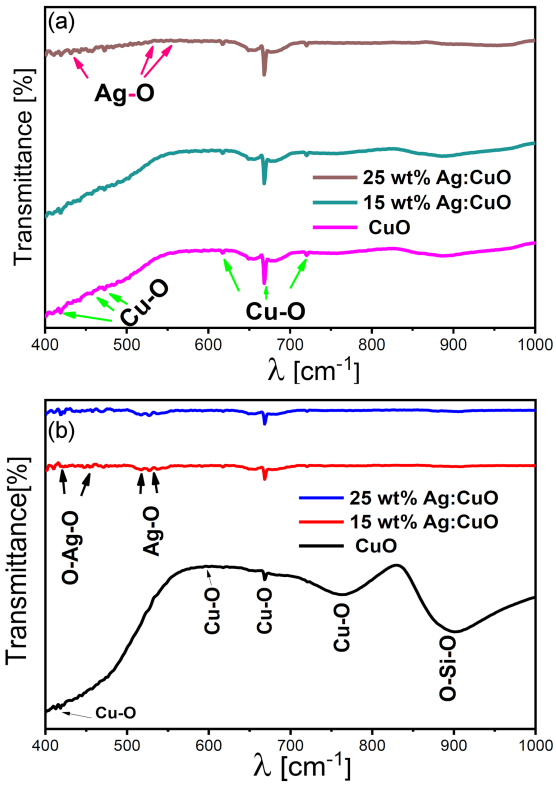

Fig. 7. Infrared spectra of CuO undoped and Ag-doped CuO deposited by (a) sol–gel dip coating and (b) sol–gel spin coating method.

25 wt% Ag in thin films deposited by dip coating (panel a) and 0.71% for doping with 15 wt% Ag and 1.52% for doping with 25 wt% in thin films deposited by spin coating (panel b), see Table II). The EDX results fit well with XRD data.

3.4. Vibration spectroscopy investigations using FT-IR

Fourier-transform infrared spectroscopy (FT-IR) characterization is used to determine the chemical properties of a material through separate vibration modes of each bond and the understanding of their chemical compositions. FT-IR spectra of thin films prepared by dip coating (a) and spin coating method (b) are recorded in the 400–1000 cm^{-1} range, as shown in Fig 7. We note that there are several modes of bond vibration found in these films, which results in the formation of copper oxide in the case of CuO and the formation of Ag_2O_3 in the case of doping. The peaks at 413, 424, 462, 478, 529, 575, 478, 529, 718, and 908 cm^{-1} characterize the Cu–O bond [39–42]. After the addition of silver, peaks at 437, 530, 708, 804, and 866 cm^{-1}, which characterize Ag–O binding, and the peak at 460 cm^{-1}, which characterizes Ag–O–Ag, were observed [43, 44].

3.5. UV-visible spectroscopy

The transmittance spectra of the thin layers prepared by the sol–gel method (dip coating) were recorded as a function of the wavelength in the range of 350–900 nm and are presented in Fig. 8a. The maximum transmittance increases with the wavelength increasing up to 90% for pure CuO and decreases down to 50% with silver doping increasing, as obtained in other works [30, 36]. The decrease of transmittance can be explained by the defects resulting from the doping which causes the scattering of the photons. Also with addition of doping, the free carriers increase and lead to an increase in light absorption. In addition, an increase in thickness between 102 and 146 nm with the increase in doping is a factor impacting the decrease in transmittance.

The optical transmission spectra of thin films of undoped and silver-doped copper oxide deposited by the sol–gel method (spin coating) on a glass substrate were recorded as a function of wavelength in the range of 200–900 nm and are presented in Fig. 3b. All the films have an average transmission of 4–12% in the visible region (400–800 nm). The transmittance decreases with the existence of doping in the range of 700–900 nm. This reveals

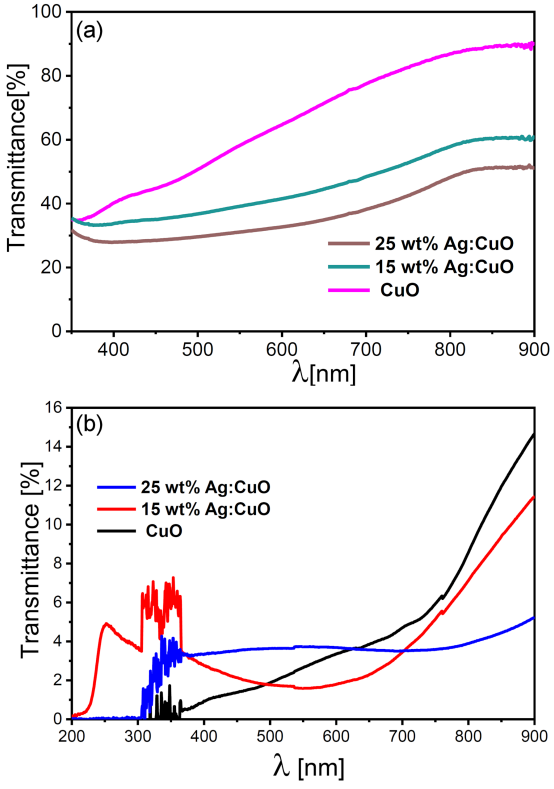

Fig. 8. Optical transmittance spectra of CuO undoped and doped with silver deposited by two methods: (a) sol–gel dip coating and (b) sol–gel spin coating.

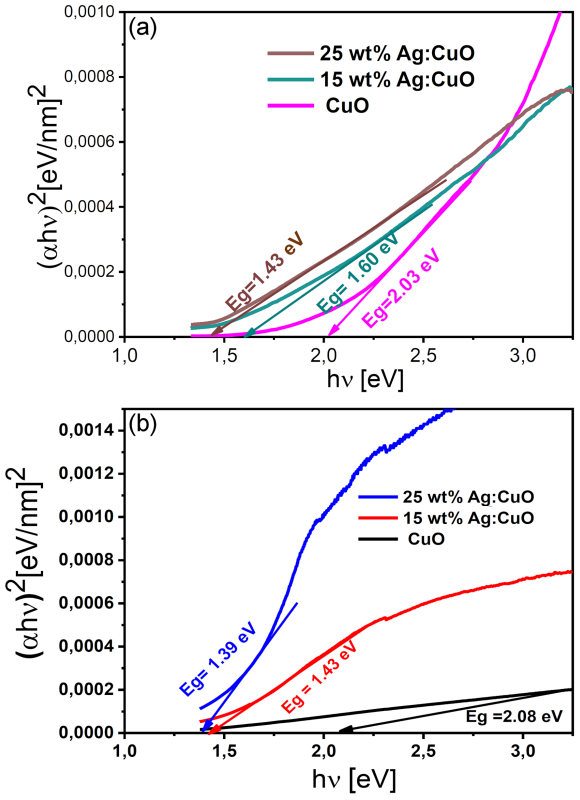

Fig. 9. Variation of $(\alpha h\nu)^2$ as a function of photon energy of copper oxide undoped and doped with silver deposited by sol–gel dip coating (a) and sol–gel spin coating (b).

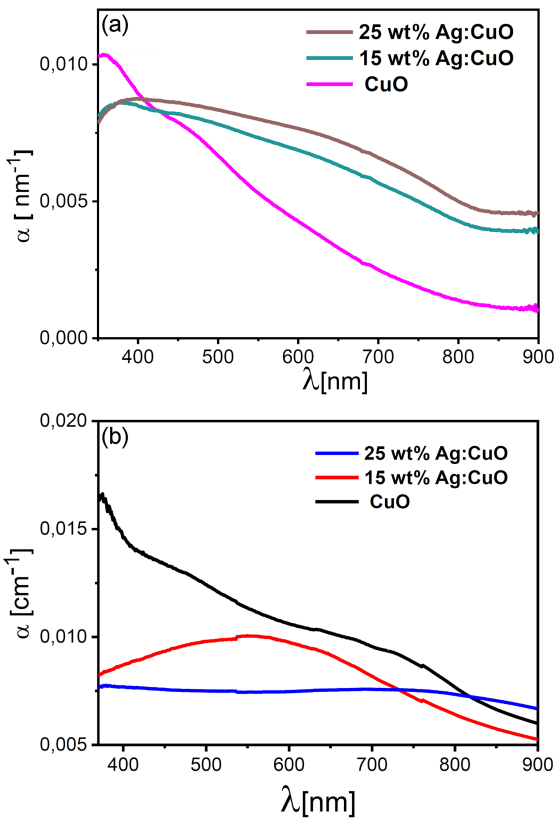

Fig. 10. Absorption coefficient as a function of wavelength of copper oxide undoped and doped, deposited by different methods: sol–gel dip coating (a) and sol–gel spin coating (b).

that there is an interaction between photons and electrons, which causes the absorption of light for the 25 wt% Ag-doped film. The higher transmittance compared to other films can be attributed to the film's surface being more homogeneous than that of the others. Thin films deposited by the dip coating method are very smooth and homogeneous compared to films deposited by spin coating. This result is well confirmed by the results of transmittance and morphology of thin films.

From the Tauc relation, the direct band gap of CuO films undoped and doped with silver was calculated by [45]

$$\alpha h\nu = A\sqrt{h\nu - E_g}. \tag{6}$$

The plot of $(\alpha h\nu)^2$ as a function of the photon energy $E = h\nu$ with the extrapolation method intersecting the tangent with the x-axis ($(\alpha h\nu)^2 = 0$) gives the optical gap E_g, as shown in Fig. 9.

In thin films prepared by the sol–gel dip coating method, the gap energy varies between 2.03–1.43 eV and decreases as doping increases. Thin films deposited by the method of sol–gel spin coating have an energy gap varying between 2.08–1.43 eV for thin films of CuO undoped and doped with 15 wt% Ag. When the doping of Ag is 25 wt%, the gap energy is 1.58 eV. This variation agrees with the results found in paper [46], with the same doping element and the same spin coating method. It has been noticed that the change in the grain size of the CuO nanostructures could be the cause of the change in E_g [47]. The inverse relationship between crystal size and gap energy can be explained by changes such as oxygen stoichiometry, quantum confinement size effect, and microcrystals of different morphologies [48–51].

In order to find the absorption coefficient (α), we used the following equation [52]

$$\alpha = \frac{1}{d}\ln\left(\frac{100}{T}\right), \tag{7}$$

where d is the thickness of the sample, and T [%] is its transmission.

Figure 10a and b shows that all films have a high α value of 10^4 cm^{-1} in the visible range, indicating direct transmission [25, 53]. The values of the absorption coefficient increase at the edge of the primary absorption towards shorter wavelengths, therefore also towards higher photon energies, increase with doping in the case of films prepared by the dip coating method, and decrease in the case of films prepared by the spin coating method.

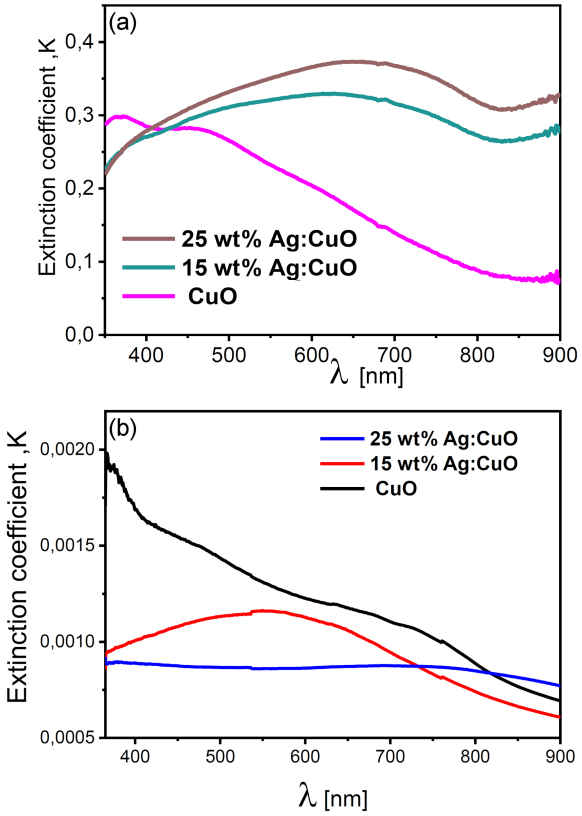

Fig. 11. Extinction coefficient as a function of wavelength of copper oxide undoped and doped with silver deposited by sol–gel dip coating (a) and sol–gel spin coating (b).

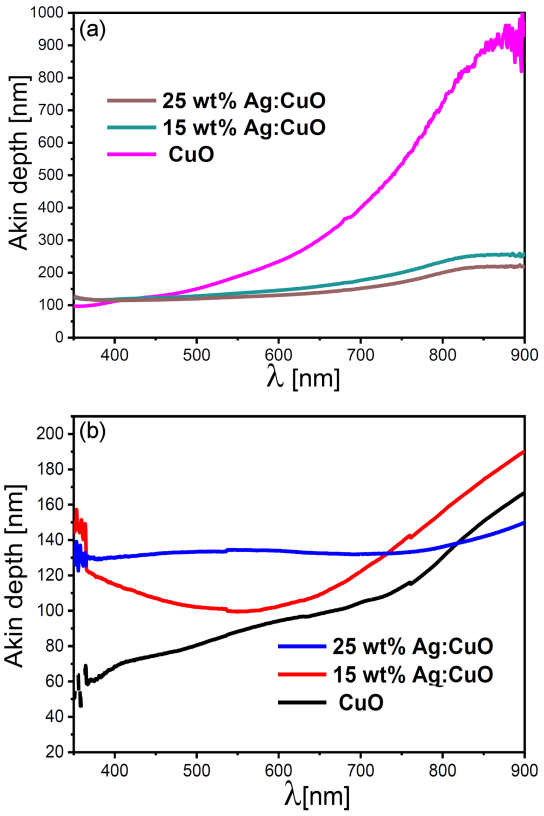

Fig. 12. Variation of skin depth as a function of wavelength of copper oxide undoped and doped with silver deposited by sol–gel dip coating (a) and sol–gel spin coating (b).

The extinction coefficient (K) is calculated by the following equation [54]

$$K = \frac{\alpha\,\lambda}{4\pi}, \tag{8}$$

where λ is the wavelength.

The spectra of the extinction coefficient as a function of wavelength are shown in Fig. 11. The extinction coefficient of thin films prepared by the dip coating method is increased with the doping increase and decreased in the case of films deposited by the spin coating method.

Skin depth (χ) is absorption depth given by the inverse of the absorption coefficient and describes how deeply light can penetrate into a semiconductor material before being fully absorbed, with the distance through which a wave penetrates into the thin film [55, 56]

$$\chi = \frac{1}{\alpha}. \tag{9}$$

Figure 12 presents the variation of skin depth as a function of wavelength. It has been noted that in the layers prepared by dip coating, the skin depth is reduced with the increase in Ag doping. This can be explained by the increase in absorption coefficient thanks to smooth surface of layers prepared by dip coating, but in the case of films prepared by the spin coating method, the skin depth increases with the increase in doping, which explains the surface roughness.

3.6. Electrical properties

The electrical properties of the thin films are measured by the four-point method.

The volume resistivity was calculated by dividing the voltage drop (V) from the two inner probes by the applied current (I) from the two outer probes and thickness (e) [57, 58].

The volume resistivity and conductivity value are computed using the formula

$$\rho = \frac{\Delta V}{I}\frac{e\pi}{\ln(2)}. \tag{10}$$

The relationship between resistivity and conductivity was shown by the following equation

$$\sigma = \frac{1}{\rho}. \tag{11}$$

Figure 13 represents the variation of the electrical conductivity of the thin films deposited by two methods: sol–gel dip coating (a) and sol–gel spin coating (b). It is observed that the electrical

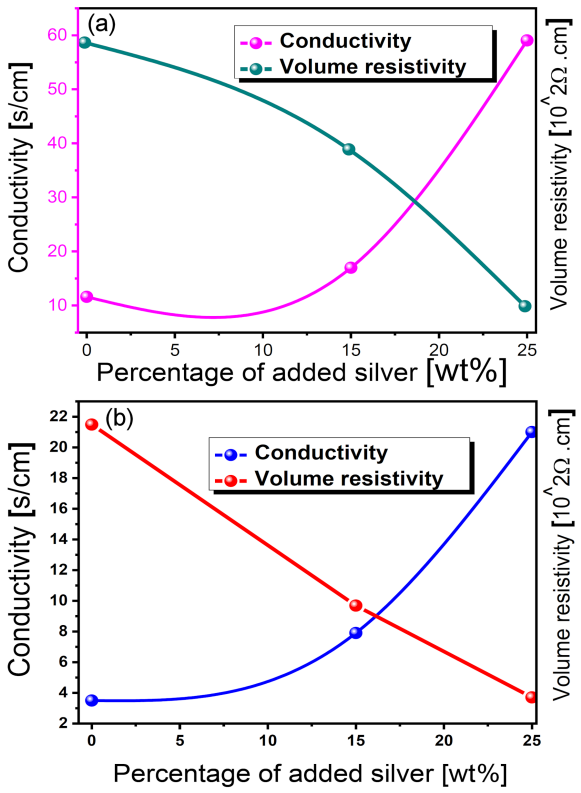

Fig. 13. Variation of conductivity and volume resistivity as a function of doping rate in two methods, i.e., sol–gel dip coating (a) and sol–gel spin coating (b).

TABLE III

Thickness and electrical conductivity of copper oxide undoped and silver-doped deposited with two method (dip coating and spin coating).

Material	Dip coating		Spin coating	
	e [nm]	σ [s/cm]	e [nm]	σ [s/cm]
CuO pure	102	11.6	320	3.5×10^{-5}
15 wt% Ag:CuO	128	16.99	412	7.9×10^{-5}
25 wt% Ag:CuO	146	59.05	443	21×10^{-5}

conductivity increases with the increase in doping with Ag in both cases. This increase can be explained by the increase in the grain size and the grain boundary decrease. As the energy gap decreases, the scattering of carriers at the grain boundaries consequently decreases [57, 59]. In addition to this effect, the thickness of CuO thin films, which acted as the active layer, was considered an important factor in studying the effect on the electrical properties [57]. In addition, the electrical conductivity of CuO films of p-type varies with the density of copper vacancies, which act as surface acceptors [60]. The electrical conductivity values of the films prepared by the dip coating method vary between 11.6 and 59.05 $(\Omega\ \mathrm{cm})^{-1}$; these values are well agreed with results in [61–62]. In films prepared by the method of spin coating, the values of the conductivity are very small compared to the other and vary between 3.5×10^{-5} and 21×10^{-5}, see Table III. They agree well with articles [15, 57].

4. Conclusions

In summary, thin layers of CuO undoped and doped with different percentages of silver and deposited with different methods (sol–gel dip coating and sol–gel spin coating) show polycrystalline in a monoclinic structure with a $C2/c$ space group. The crystallite size of thin films deposited by dip coating was calculated by Scherrer's formula and varied between 20 and 29 nm. The morphology of the films is porous, uniform, and dense. From the transmission spectra, the gap energy changes between 1.43 and 2.03 eV, and the average transmission between 350 and 900 nm is 90% to 50%, and electrical conductivity varied between 11–59 $(\Omega\ \mathrm{cm})^{-1}$ decrease with the increased doping. But in thin films deposited by spin coating, we have a difference in crystallite size between 24 and 33 nm and gap energy change between 1.39 and 2.08 eV, and the average transmission between 350–900 nm is 12% to 4%. The electrical conductivity varied between 3.5×10^{-5} and 21×10^{-5} $(\Omega\ \mathrm{cm})^{-1}$. We checked the existence of Cu–O and Ag–O absorption bands by the FT-IR method. The morphology of the films is uniform and dense with nano-spherical shape. We notice a clear change in the morphological, optical, and electrical properties with the effect of different deposited methods and Ag doping of CuO. We conclude that thin films deposited by the sol–gel spin coating technique are excellent for generating high-quality homogeneous and uniform thin films. It is suitable for solar cell applications and gas sensors.

Acknowledgments

This work has been supported by the Laboratory of Research of the Physico-Chemistry of Surfaces and Interfaces (LRPCSI), 20 Août 1955 University Skikda. The Laboratory of MOLTECH-Anjou, Angers University, France, has supported this work.

References

[1] Ş. Baturay, *Acad. Platform J. Eng. Sci.* **8**, 84 (2020).

[2] V. Patil, D. Jundale, S. Pawar, M. Chougule, P. Godse, S. Patil, B. Raut, S. Sen, *J. Sens. Technol.* **1**, 36 (2011).

[3] P. Samarasekara, N.T.R.N. Kumara, N.U.S. Yapa, *J. Phys. Condens. Matter* **18**, 2417 (2006).

[4] B. Dikra, M. Fellah, R. Barille S. Weiß, M.A. Samad, A. Alburaikan, H. Abd El-Wahed khalifa, A. Obrosov, *J. Sci. Adv. Mater. Devices* **9**, 100642 (2023).

[5] A. Rydosz, *Coatings* **8**, 425 (2018).

[6] U.R. Shwetha, M.A. Alnuwaiser, M.S. Latha, V.S. Betageri, V.A. Shilpa, M.I. Khan, K. Guedri, *J. Indian Chem. Soc.* **99**, 100606 (2022).

[7] O. Diachenko, J. Kováč Jr., O. Dobrozhan, P. Novák, J. Kováč, J. Skriniarova, A. Opanasyuk, *Coatings* **11**, 1392 (2021).

[8] L. Sun, Y. Zhuang, Y. Yuan, W. Zhan, X.-J. Wang, X. Han, Y. Zhao, *Adv. Energy Mater.* **9**, 1902839 (2019).

[9] T. Oku, R. Motoyoshi, K. Fujimoto, T. Akiyama, B. Jeyadevan, J. Cuya, *J. Phys. Chem. Solids* **72**, 1206 (2011).

[10] G. Varughese, V. Rini, S.P. Suraj, K.T. Usha, *Adv. Mater. Sci.* **14**, 49 (2014).

[11] M. Nesa, M. Sharmin, K.S. Hossain, A.H. Bhuiyan, *J. Mater. Sci. Mater. Electron.* **28**, 12523 (2017).

[12] E. Benrezgua, B. Deghfel, A. Zoukel, W.J. Basirun, R. Amari, A. Boukhari, M.K. Yaakob, S. Kheawhom, A.A. Mohamad, *J. Mol. Struct.* **1267**, 133639 (2022).

[13] N. Al Armouzi, G. El Hallani, A. Liba, M. Zekraoui, H.S. Hilal, *Mater. Res. Express* **6**, 116405 (2019).

[14] M. Asadi, S.M. Rozati, *Mater. Sci. Pol.* **35**, 355 (2017).

[15] S. Kose, F. Atay, V. Bilgin, I. Akyuz, *Mater. Chem. Phys.* **111**, 351 (2008).

[16] F.A. Akgul, G. Akgul, N. Yildirim, H.E. Unalan, R. Turan, *Mater. Chem. Phys.* **147**, 987 (2014).

[17] Y. Du, X. Gao, X. Zhang, X. Meng, *Phys. B Condens. Matter* **546**, 28 (2018).

[18] F. Bayansal, T. Taşköprü, B. Şahin, H.A. Çetinkara, *Metall. Mater. Trans. A* **45**, 3670 (2014).

[19] K. Khojier, H. Savaloni, Z. Sadeghi, *J. Theor. Appl. Phys.* **8**, 116 (2014).

[20] F. Peng, Y. Sun, Y. Lu, W. Yu, M. Ge, J. Shi, R. Cong, J. Hao, N. Dai, *Nanomaterials* **10**, 774 (2020).

[21] A. Sharma, Y. Kumar, P.M. Shirage, *J. Mater. Sci. Mater. Electron.* **29**, 10769 (2018).

[22] A. Rydosz, W. Maziarz, T. Pisarkiewicz, K. Wincza, S. Gruszczyński in: *2013 Int. Conf. Informatics*, Electron Vision (ICIEV), IEEE, 2013.

[23] J. Lillo-Ramiro, J.M. Guerrero-Villalba, M. de L. Mota-González, F.S. Aguirre-Tostado, G. Gutiérrez-Heredia, I. Mejía-Silva, A. Carrillo-Castillo, *Optik* **229**, 166238 (2021).

[24] D. Prasanth, K.P. Sibin, H.C. Barshilia, *Thin Solid Films* **673**, 78 (2019).

[25] D. Bouras, M. Fellah, M.A. Habeeb, L. Aouar, R. Barille, G.A. El-Hiti, *J. Korean Ceram. Soc.* **61**, 837 (2024).

[26] H. Faiz, K. Siraj, M.F. Khan, M. Irshad, S. Majeed, M.S. Rafique, S. Naseem, *J. Mater. Sci. Mater. Electron.* **27**, 8197 (2016).

[27] R. Ivanauskas, A. Kunciute, I. Ancutiene, M. Andrulevicius, *Surf. Interfaces* **28**, 101675 (2022).

[28] N. Srinatha, P. Raghu, H.M. Mahesh, B. Angadi, *J. Alloys Compd.* **722**, 888 (2017).

[29] G. Durai, P. Kuppusami, K. Viswanathan, *J. Mater. Sci. Mater. Electron.* **29**, 2051 (2018).

[30] M. Zerouali, R. Daïra, B. Boudjema, R. Barillé, D. Bouras, S. Iaiche, *Digest J. Nanomater. Biostruct.* **18**, 1371 (2023).

[31] Z. Madiha, D. Radouane, B. Dikra, B. Boudjema, R. Barille, *J. Nano Res.* **80**, 1 (2023).

[32] H, Absike, Z. Essalhi, H. Labrim, B. Hartiti, N. Baaalla, M. Tahiri, B. Jaber, H. Ezzahraouy, *Opt. Mater.* **118**, 111224 (2021).

[33] A. Bougharouat, N. Touka, D. Talbi, K. Baddari, *Ann. Chim.* **45**, 439 (2021).

[34] S. Das, T.L. Alford, *J. Appl. Phys.* **113**, 244905 (2013).

[35] K.K.P. Kumar, N.D. Dinesh, S.K. Murari, *Int. J. Nano Biomater.* **8**, 314 (2019).

[36] S.M.A. Al-dujayli, N.A. Ali, *J. Ovonic Res.* **18**, 579 (2022).

[37] R.M. Thyab, M.A.H. Al-Hilo, F.A. Yasseen, H. Alshater, E.G. Blall, M.A. Abdel-Lateef, *NeuroQuantology* **20**, 99 (2022).

[38] R.D. Prabu, S. Valanarasu, I. Kulandaisamy, V. Ganesh, M. Shkir, A. Kathalingam, *J. Mater. Sci. Mater. Electron.* **28**, 6754 (2017).

[39] M. Zerouali, D. Bouras, R. Daira, M. Fellah, B. Boudjema, R. Barille, E.-F. Sakher, S. Bellucci, G.A. El-Hiti, *Opt. Mater.* **152**, 115495 (2024).

[40] B.T. Sone, A. Diallo, X.G. Fuku, A. Gurib-Fakim, M. Maaza, *Arab. J. Chem.* **13**, 160 (2020).

[41] N.M. Umran, A.M.A. Majeed Z.S. Sultan, *J. Phys. Conf. Ser.* **1279**, 012078 (2019).

[42] A.H. Alami, M. Faraj, K. Aokal, A.A. Hawili, M. Tawalbeh, D. Zhang, *Nanomaterials* **10**, 784 (2020).

[43] B. Dikra, M. Fellah, R. Barille, M.A. Samad, M. Rasheed, M.A. Alreshidi, *Opt. Quant. Electron.* **56**, 104 (2024).

[44] S.M. Hosseini, I. Abdolhosseini Sarsari, P. Kameli, H. Salamati, *J. Alloys Compd.* **640**, 408 (2015).

[45] A. Moumen, B. Hartiti, E. Comini, Z. El khalidi, H.M.M. Munasinghe Arachchige, S. Fadili, P. Thevenin, *Superlattices Microstruct.* **127**, 2 (2019).

[46] A.A.I. Khalil, A.-S.H.M. Abd El-Gawad, A.-S. Gadallah, *Opt. Mater.* **109**, 110250 (2020).

[47] H. Güney, D. Iskenderoglu, M.E. Güldüren, K.Ç. Demïr, S.M. Karadeniz, *Opt. Mater.* **132**, 112869 (2022).

[48] R. Nitta, Y. Kubota, T. Kishi, N. Matsushita, *Thin Solid Films* **762**, 139555 (2022).

[49] M.H. Kabir, H. Ibrahim, S.A. Ayon, M.M. Billah, S. Neaz, *Heliyon* **8**, 10609 (2022).

[50] J. Uddin, M. Sharmin, M.N. Hasan, J. Podder, *Opt. Mater.* **119**, 111388 (2021).

[51] R. Marnadu, M. Shkir, J. Hakami, I.M. Ashraf, P. Baskaran, D. Sivaganesh, K.V. Chandekar, W.K. Kim, S. Gedi, *Surf. Interfaces* **34**, 102366 (2022).

[52] A.M. El Sayed, M. Shaban, *Spectrochim. Acta A* **149**, 638 (2015).

[53] S. Dridi, E. Aubry, N. Bitri, F. Chaabouni P. Briois, *Coatings* **10**, 963 (2020).

[54] B. Dikra, M. Fellah, A. Mecif, R. Barillé, A. Obrosov, M. Rasheed, *J. Korean Ceram. Soc.* **60**, 155 (2023).

[55] Z.N. Kayani, H. Aslam, *Adv. Powder Technol.* **32**, 2345 (2021).

[56] Z.N. Kayani, W. Chaudhry, R. Sagheer, S. Riaz, S. Naseem, *Mater. Sci. Eng. B* **283**, 115799 (2022).

[57] R. Sharma, Himanshu, S.L. Patel, M.D. Kannan, M.S. Dhaka, *Surf. Interfaces* **33**, 102204 (2022).

[58] N.A. Raship, M.Z. Sahdan, F. Adriyanto, M.F. Nurfazliana, A.S. Bakri, *AIP Conf. Proc.* **1788**, 030121 (2017).

[59] S.S. Shariffudin, S.S. Khalid, N.M. Sahat, M.S.P. Sarah, H. Hashim, *Mater. Sci. Eng.* **99**, 012007 (2015).

[60] E.C. Nwanna, P.E. Imoisili, S.O. Bitire, T.-C. Jen, *Coatings* **11**, 1545 (2021).

[61] F.Z. Chafi, L. Bahmad, N. Hassanain, B. Fares, L. Laanab, A. Mzerd, arXiv:1807.09697 (2018).

[62] R. Daira, B. Boudjema, *J. Intense Pulsed Lasers Appl. Adv. Phys.* **5**, 1 (2015).